DEVELOPMENT OF A MECHANISTIC EVALUATION METHOD FOR WASTAGE ENVIRONMENT UNDER SODIUM-WATER REACTION ACCIDENT

A. Uchibori and H. Ohshima
Japan Atomic Energy Agency
4002 Narita, Oarai, Ibaraki 311-1393, Japan
uchibori.akihiro@jaea.go.jp; ohshima.hiroyuki@jaea.go.jp

ABSTRACT

When pressurized water or vapor leaks from a failed heat transfer tube in a steam generator of sodium-cooled fast reactors, a high-velocity, high-temperature jet with sodium-water chemical reaction may cause wastage on the adjacent tubes. For assessment of the wastage environment, a mechanistic computer code called SERAPHIM calculating compressible multicomponent multiphase flow with sodium-water chemical reaction has been developed. In this study, the numerical models for liquid droplet entrainment from an interface of the reacting jet and its transport were newly developed to evaluate the environment of liquid droplet impingement erosion. The conservation equations for the liquid droplet and the source term representing an entrainment rate were integrated into the existing governing equations of the SERAPHIM code. Applicability of the SERAPHIM code, which integrates the existing and the newly developed numerical models, was investigated through the analyses of some related experiments. In the numerical analysis of the experiment on liquid droplet entrainment at the surface of the water pool, the calculated pressure at the point located upstream of the entrainment section increased with generation of the liquid droplet and then decreased to the level near the initial state. The triangle waveform of the calculated pressure was consistent with the experimental result. The experiment on water vapor discharging in liquid sodium under actual condition of the steam generator was also analyzed in the present work. The calculated temperature distribution agreed with the measurement result well. The region with higher impingement velocity of the liquid droplet was close to the wastage region confirmed in the experiment.

KEYWORDS
Sodium-cooled fast reactor, Steam generator, Sodium-water reaction, Liquid droplet entrainment, Mechanistic numerical method

1. INTRODUCTION

In a steam generator (SG) of sodium-cooled fast reactors, heat exchange takes place between liquid sodium in a shell side and water inside a heat transfer tube. When pressurized water or vapor leaks from a failed heat transfer tube, a high-velocity, high-temperature, and corrosive jet with sodium-water chemical reaction is formed in the shell side (see Fig. 1). It is known that the reacting jet may cause wastage on the adjacent tubes. Wastage is attributed to erosion, flow accelerated corrosion (FAC) or combination of them. Significant progress of wastage and degradation of a mechanical strength by temperature elevation may result in secondary failure (failure propagation) on the adjacent tubes. Failure propagation will lead to expansion of the damage and long-term shutdown of the plant. Prevention of failure propagation is a key issue in designing the SG.

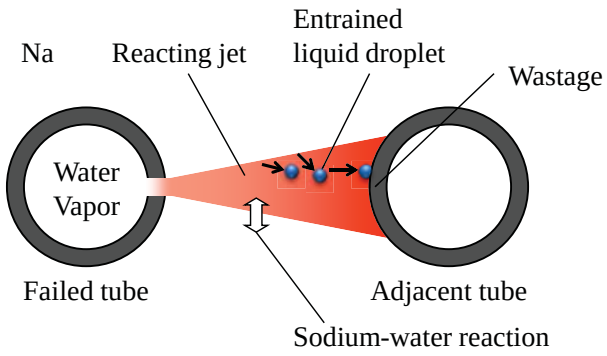

Figure 1. Reacting jet under tube failure accident.

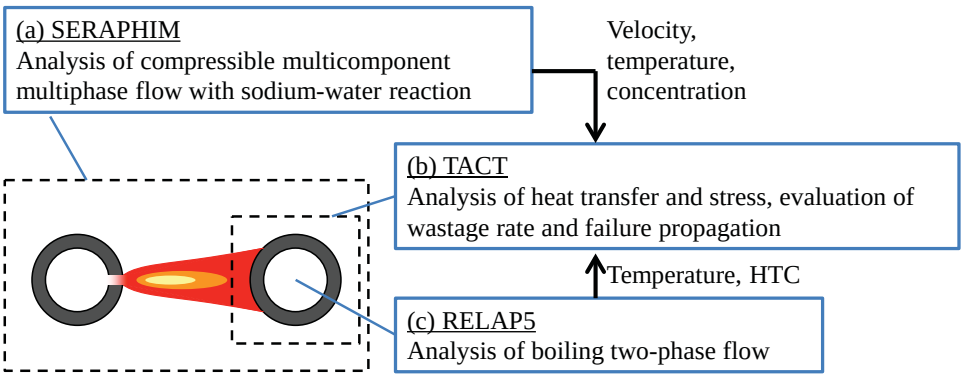

Figure 2. Multiphysics evaluation system for tube failure accident.

Numerical analysis is a most effective way for evaluating possibility of failure propagation occurrence. It has a great advantage over a mock-up experiment in aspects of a cost, development period, and versatility. In our study, a multiphysics evaluation system comprising the multiple computer codes has been newly developed (see Fig. 2). As one component of the system, there is a computer code called SERAPHIM (Sodium-watEr Reaction Analysis : PHysics of Interdisciplinary Multi-phase flow) calculating compressible multicomponent multiphase flow with sodium-water chemical reaction [1-4]. The SERAPHIM code is based on the mechanistic numerical models and predicts profiles of the velocity, temperature and concentration. In our previous studies, a multifluid model considering compressibility was adopted to calculate the multiphase flow with water, liquid sodium and multicomponent gas. A numerical model for chemical reaction which occurs at the interface between water vapor and liquid sodium has also already been developed.

Liquid sodium is entrained into the high-velocity gaseous flow from the gas-liquid interface and impinges on the adjacent tubes continuously (see Fig. 1). A liquid droplet impingement erosion (LDIE) is thought to be one of the main causes of the wastage. Kudo et al. [5] carried out the experiment on a submerged gaseous jet in liquid sodium. They visualized the liquid droplets impinging on an adjacent glass tube. Arae et al. [6] conducted the experiment on a liquid droplet impingement on the selected material and confirmed wastage on the impinging surface. Their experiments imply occurrence of the LDIE.

In this study, the numerical models for liquid droplet entrainment and its transport were newly developed to evaluate the environment of the LDIE. Applicability of the SERAPHIM code, which integrates the

existing and the newly developed numerical models, was investigated through the numerical analyses of some related experiments. Epstein et al. [7] conducted the experiment on liquid droplet entrainment at the surface of a water pool in a rectangular flow channel. Their experiment was chosen as a validation problem. In addition, the experiment on water vapor discharging in liquid sodium was analyzed to investigate applicability of the code to the actual condition of the SG.

2. NUMERICAL METHODS

2.1. Governing Equations

The multiphase flow under the tube failure accident is calculated by the multifluid model considering compressibility. The first phase is a multicomponent gas with water vapor, sodium hydroxide (NaOH) aerosol, hydrogen, sodium vapor and NaOH vapor. The second phase is liquid sodium. Liquid sodium is entrained into the gaseous flow. We considered the entrained liquid droplets as a third phase and added the governing equations for the liquid droplet phase to the existing equations. Governing equations for the three phases are as follows:

Equation of mass conservation

$$\frac{\partial}{\partial t}\left(\alpha_g \rho_g\right)+\nabla\cdot\left(\alpha_g \rho_g \mathbf{u}_g\right)=\Gamma_l^e+\Gamma_d^e-\Gamma^c+G_l^{sf}+G_d^{sf}+G^{dif} \tag{1}$$

$$\frac{\partial}{\partial t}\left(\alpha_l \rho_l\right)+\nabla\cdot\left(\alpha_l \rho_l \mathbf{u}_l\right)=-\Gamma_l^e+\Gamma^c-G_l^{sf}-S^e+S^d \tag{2}$$

$$\frac{\partial}{\partial t}\left(\alpha_d \rho_d\right)+\nabla\cdot\left(\alpha_d \rho_d \mathbf{u}_d\right)=-\Gamma_d^e-G_d^{sf}+S^e-S^d \tag{3}$$

Equation of momentum conservation

$$\begin{aligned}\frac{\partial}{\partial t}\left(\alpha_g \rho_g \mathbf{u}_g\right)+\nabla\cdot\left(\alpha_g \rho_g \mathbf{u}_g \mathbf{u}_g\right)=&-\alpha_g\nabla p+\nabla\cdot\left(\alpha_g \boldsymbol{\tau}_g\right)+\alpha_g \rho_g \mathbf{g}\\&+\mathbf{F}_{gl}^d+\mathbf{F}_{gd}^d+\Gamma_l^e \mathbf{u}_l+\Gamma_d^e \mathbf{u}_d-\Gamma^c \mathbf{u}_g+G_l^{sf}\mathbf{u}_l+G_d^{sf}\mathbf{u}_d+G^{dif}\mathbf{u}_g\end{aligned} \tag{4}$$

$$\frac{\partial}{\partial t}\left(\alpha_l \rho_l \mathbf{u}_l\right)+\nabla\cdot\left(\alpha_l \rho_l \mathbf{u}_l \mathbf{u}_l\right)=-\alpha_l\nabla p+\nabla\cdot\left(\alpha_l \boldsymbol{\tau}_l\right)+\alpha_l \rho_l \mathbf{g}-\mathbf{F}_{gl}^d-\Gamma_l^e \mathbf{u}_l+\Gamma^c \mathbf{u}_g-G_l^{sf}\mathbf{u}_l-S^e\mathbf{u}_l+S^d\mathbf{u}_d \tag{5}$$

$$\frac{\partial}{\partial t}\left(\alpha_d \rho_d \mathbf{u}_d\right)+\nabla\cdot\left(\alpha_d \rho_d \mathbf{u}_d \mathbf{u}_d\right)=-\alpha_d\nabla p+\alpha_d \rho_d \mathbf{g}-\mathbf{F}_{gd}^d-\Gamma_d^e \mathbf{u}_d-G_d^{sf}\mathbf{u}_d+S^e\mathbf{u}_l-S^d\mathbf{u}_d \tag{6}$$

Equation of energy conservation

$$\begin{aligned}\frac{\partial}{\partial t}\left(\alpha_g \rho_g h_g\right)+\nabla\cdot\left(\alpha_g \rho_g h_g \mathbf{u}_g\right)=&\alpha_g\frac{Dp}{Dt}+\alpha_g\Phi_g+\nabla\cdot\left(\alpha_g \lambda_g \nabla T_g\right)\\&+a_{gl}H_{gl}\left(T_l-T_g\right)+a_{gd}H_{gd}\left(T_d-T_g\right)\\&+\Gamma_l^e\left(h_l+i_l\right)+\Gamma_d^e\left(h_d+i_d\right)-\Gamma^c h_{gy}+Q^{sf}+Q^{dif}\end{aligned} \tag{7}$$

$$\begin{aligned}\frac{\partial}{\partial t}\left(\alpha_l \rho_l h_l\right)+\nabla\cdot\left(\alpha_l \rho_l h_l \mathbf{u}_l\right)=&\alpha_l\frac{Dp}{Dt}+\alpha_l\Phi_l+\nabla\cdot\left(\alpha_l \lambda_l \nabla T_l\right)+a_{gl}H_{gl}\left(T_g-T_l\right)\\&-\Gamma_l^e\left(h_l+i_l\right)+\Gamma^c h_{gy}-G_l^{sf}h_l-S^e h_l+S^d h_d\end{aligned} \tag{8}$$

$$\frac{\partial}{\partial t}\left(\alpha_d \rho_d h_d\right)+\nabla\cdot\left(\alpha_d \rho_d h_d \mathbf{u}_d\right)=\alpha_d\frac{Dp}{Dt}+a_{gd}H_{gd}\left(T_g-T_d\right)-\Gamma_d^e\left(h_d+i_d\right)-G_d^{sf}h_d+S^e h_l-S^d h_d \tag{9}$$

where α is the volume fraction, ρ the density, $\mathbf{u}$ the velocity vector, Γ^e the evaporation rate, Γ^c the condensation rate, G^{sf} the mass generation rate by surface reaction, G^{dif} the source term by species diffusion, S^e the droplet entrainment rate, p the pressure, $\boldsymbol{\tau}$ the viscous stress tensor, $\mathbf{g}$ the gravity vector, $\mathbf{F}^d$ the interfacial drag force, h the enthalpy, Φ the dissipation function, λ the thermal conductivity, T the temperature, a the interfacial area density, H the coefficient of heat transfer, i the latent heat, h_{gy} the enthalpy of the species, Q^{sf} the heat generation rate by surface reaction, and Q^{dif} the source term by species diffusion. Subscript g stands for the gas phase, l the liquid phase and d the liquid droplet phase. Equations (3), (6), and (9) were newly introduced in the present work. The equation of state and the advection-diffusion equation for each species are also considered in addition to Eqs. (1) to (9).

The time-derivative terms in Eqs. (1) to (9) were approximated by the forward difference scheme. The convective and diffusion terms were estimated explicitly. The second-order TVD scheme was chosen for the convective terms in the equation of momentum conservation to reproduce the structure of an underespanded jet [4]. The convective terms in other equations were discretized by the first-order upwind difference scheme. The second-order central difference scheme was applied to the viscous, heat conduction and diffusion terms.

The governing equations are solved by the HSMAC (Highly Simplified Marker And Cell) method modified for compressible multiphase flows [3, 4]. The HSMAC method for incompressible single-phase flow was developed by Hirt and Cook [8]. In this method, the pressure and the velocity are corrected so as to satisfy continuity by using the Newton-Raphson method. The HSMAC method is very useful for parallel computation because there is no need to solve a simultaneous linear equation.

2.2. Liquid Droplet Entrainment Model

To estimate the liquid droplet entrainment rate appearing as a source term in the governing equations, we applied a Ricou-Spalding's law [9]:

$$m_e = E_0 \left(\rho_g \rho_l \right)^{1/2} \left| \mathbf{u}_g - \mathbf{u}_l \right| \tag{10}$$

where m_e is the liquid droplet entrainment rate and E_0 the empirical constant. Liquid droplet entrainment by submerged gaseous jets was investigated in several studies [10-13]. All these studies demonstrated that the liquid droplet entrainment rate could be represented well by the similar formula with Eq. (10). Epstein et al. [7] demonstrated that the liquid droplet entrainment rate derived from the theoretical equation considering the Kelvin-Helmholtz instability takes same functional form as Eq. (10). From their derivation, it is shown that the empirical constant E_0 includes the effect of the surface tension. Epstein et al. estimated the value of the empirical constant E_0 for each of the fluid sets by using the theoretical model [7, 14]. For one example, they proposed $E_0 = 0.14$ for the air-water system and $E_0 = 0.08$ for the water vapor-liquid sodium system under the actual condition of the SG. The values estimated by Epstein et al. were adopted also in our numerical model. In this study, the numerical model integrating Eq. (10) and the transport equation were validated through the after-mentioned numerical analysis.

The drag force between the gas and the entrained liquid droplet is given by

$$\mathbf{F}_{gd}^d = -\frac{3}{4}\frac{1}{D}\alpha_d \rho_g C_D \left| \mathbf{u}_g - \mathbf{u}_d \right| \left(\mathbf{u}_g - \mathbf{u}_d \right) \tag{11}$$

Walsh proposed the following correlation for a drag coefficient of moving solid particles in a supersonic gaseous flow [15].

$$C_D = \frac{24}{\mathrm{Re}}\left(1 + 0.15\,\mathrm{Re}^{0.687}\right)\left[1 + \exp\left(-\frac{0.427}{M_r^{4.63}} - \frac{3}{\mathrm{Re}^{0.88}}\right)\right] \tag{12}$$

$$M_r = \frac{\left|\mathbf{u}_g - \mathbf{u}_d\right|}{\sqrt{\gamma R T_g}} \tag{13}$$

where γ is the specific heat ratio and R the universal gas constant. We considered the liquid droplet as a sphere and applied Eqs. (12) and (13) to the drag coefficient C_D in Eq. (11). Epstein et al. [16] measured the diameter of the liquid droplet entrained by the gaseous jet and derived the following correlation describing Sauter mean diameter (SMD).

$$\frac{\mathrm{SMD}}{d_0} = 0.39\left(\frac{\sigma}{u_0^2 \rho_0 d_0}\right)^{0.4} \tag{14}$$

where d_0, u_0, and ρ_0 are the diameter, velocity, and density of the gaseous jet after underexpansion. σ is the surface tension. To estimate the drag force represented by Eq. (11), we calculated the diameter of the liquid droplet from Eq. (14).

2.3. Chemical Reaction Model

The mass generation rate by the chemical reaction at the interface between water vapor and liquid sodium is calculated by a surface reaction model developed in our previous studies. The formulation of the surface reaction model is outlined below.

The following reaction is dominant between water vapor and liquid sodium [1, 2].

$$\mathrm{Na} + \mathrm{H_2O} \rightarrow \mathrm{NaOH} + \frac{1}{2}\mathrm{H_2} \tag{15}$$

The surface reaction model is based on the assumption of infinite reaction rate. In other words, progress of the chemical reaction at the gas-liquid interface is limited by the mass flow rate of the reactant gas toward the interface. The mass flow rate of the reactant gas j is written as

$$\gamma_j^{sf} = Sh\frac{D_{mj}}{l}\rho_g Y_j a \tag{16}$$

where Sh is the Sherwood number, l the characteristic length. Equation (16) includes some unknown parameters. Considering an analogy between heat and mass transfer, Eq. (16) is rewritten as

$$\gamma_j^{sf} = -Le^{b-1}\frac{H_{gl}}{C_{pg}}Y_j a \tag{17}$$

where Le is the Lewis number, b the empirical constant and C_{pg} the gas-phase constant pressure specific heat. The Lewis number is calculated according to its definition. The empirical constant b was set to 0 in our model since there is the knowledge that b is not so effective on the reacting zone [17]. Tanabe et al. conducted the experiment on water vapor leakage into liquid sodium and reported that the coefficient of heat transfer on the surface of a heat transfer tube in a reacting zone was approximately 10000 W/m^2/K

[18]. Heat transfer on the gas-liquid interface seems to be similar to that on the tubes because the liquid-phase velocity is much smaller than the gas-phase velocity. For this reason, we applied the coefficient of heat transfer measured on the tube to that on the gas-liquid interface. The interfacial area density *a* is given by a Nigmatulin model [19]. We have supposed that the reaction products, NaOH and hydrogen, move to the gas phase. Therefore, the SERAPHIM code considers the multicomponent gas phase.

3. NUMERICAL ANALYSIS

3.1. Numerical Analysis of Liquid Droplet Entrainment

Applicability of the liquid droplet entrainment and transport model was investigated through the numerical analysis of the experiment by Epstein et al. [7]. Figure 3 shows a schematic of the experiment. The experimental apparatus consists of the high-pressure air tank, the rupture disk and the rectangular flow channel 100 mm both in width and height. There is an expanded part (reservoir) 50 mm in depth at the middle of the flow channel. The reservoir is initially filled with the water to the floor level of the flow channel. The pressurized air goes into the flow channel through the rupture disk and entrains the liquid droplet from the surface of the water pool. The pressure variation at the point located upstream of the entrainment section was recorded. As shown in Fig. 4, we consider the three-dimensional computational domain simulating the region from the rupture disk to the end of the channel. Two different conditions were analyzed. In the case 1, the reservoir is initially filled with the water at 20 °C and hydrostatic pressure as with the experiment. The air at 20 °C and 0.1 MPa exists in the computational domain except for the reservoir. In the case 2, the air at the same conditions fills whole domain. This means single-phase gaseous flow in the same flow channel. In both cases, the pressurized air goes into the region from the inflow boundary corresponding to the rupture disk. The stagnation pressure was set to 0.69 MPa. We considered the critical state at the inflow boundary and decided the boundary conditions from the well-known relationships derived from the assumption of an isentropic flow. The pressure at the end of the channel was set to be constant at 0.1 MPa. The gas, liquid and liquid droplet phases can go out from the end of the channel. The computational domain was divided into the equally-spaced mesh with a cell 5 mm on a side.

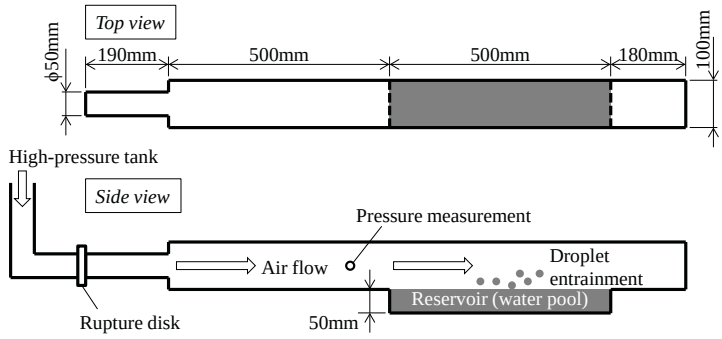

Figure 3. Schematic of liquid droplet entrainment experiment by Epstein et al. [7]

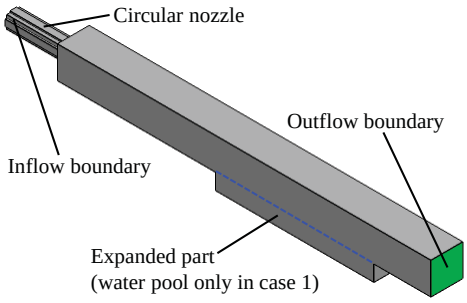

Figure 4. Computational domain for liquid droplet entrainment.

An underexpanded jet appears when an ambient pressure is lower than a critical pressure. In the case of 0.69 MPa of the stagnation pressure, the critical pressure becomes about 0.36 MPa and is higher than the ambient pressure (0.1 MPa). Figure 5 shows the instantaneous distributions of the pressure on the vertical plane at the center of the computational domain. It can be seen that the air expands after exiting the circular nozzle and a shock wave called Mach disk appears at 0.02 seconds in both cases. The numerical

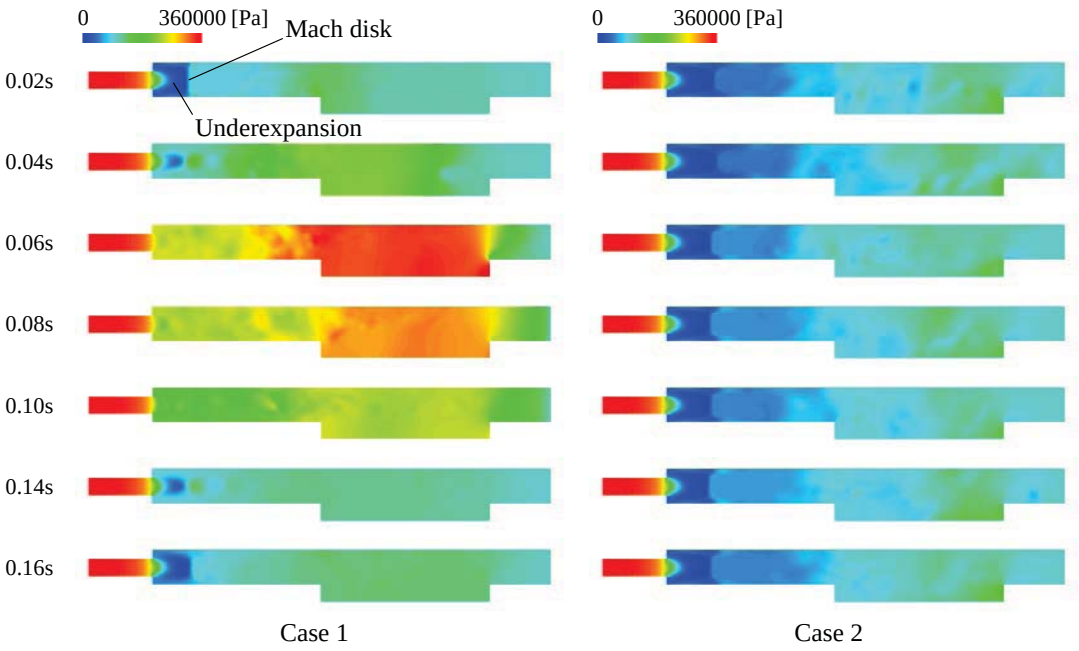

Figure 5. Distribution of pressure.

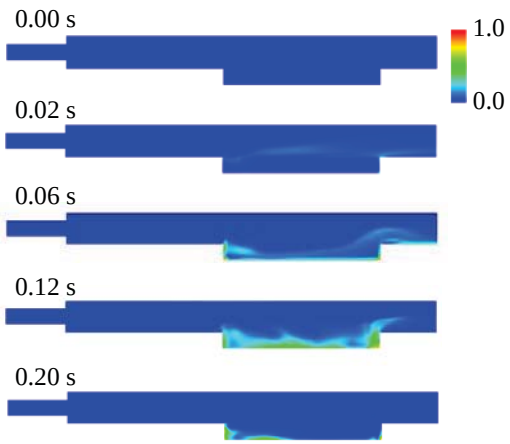

Figure 6. Distribution of volume fraction of liquid droplet.

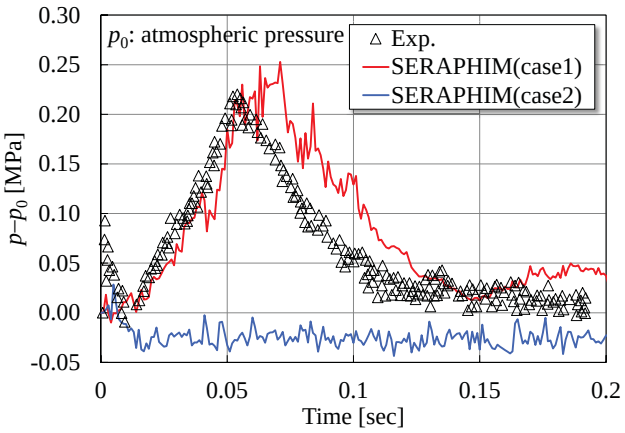

Figure 7. Comparison of pressure variation.

result shown in Fig. 5 represents the well-known structure of the underexpanded jet. Only in the case 1, the underexpanded jet disappeared gradually and then appeared from 0.14 seconds again. The pressure increased around the reservoir and reached to the peak at about 0.06 seconds. The pressure rise shown in Fig. 5 is the cause of the disappearance of the underexpanded jet.

The pressure rise is related to liquid droplet entrainment. Figure 6 shows the instantaneous distributions of the volume fraction of the liquid droplet. The numerical result showed that the liquid droplet appeared above the water pool. At 0.2 seconds, almost no liquid phase remains in the reservoir. The time period to be almost empty of the reservoir in the numerical analysis roughly agrees with the experimental observation by a video camera which has one video frame of about 40 ms. The pressure at the point located upstream of the reservoir is shown in Fig. 7. The pressure in the case 1 increased with generation

of the liquid droplet and then decreased to the level near the initial state. This behavior can be confirmed also in Fig. 5. The triangle waveform of the calculated pressure shows good agreement with the experimental result. The pressure rise during the first half is due to the action of the entrained liquid droplet as a drag against the air flow. The pressure subsequently decreased with outflow of the liquid droplet. The numerical analysis in the case 2 showed no increase of the pressure. This result is consistent with the experimental one described in the paper by Epstein et al. [7]. The numerical analysis reproduced the pressure variation both in the two cases, implying basic applicability of the proposed numerical models to the liquid droplet entrainment and transport phenomena.

3.2. Numerical Analysis of Water Vapor Discharging in Liquid Sodium

Applicability of the SERAPHIM code, which integrates the above-mentioned numerical models, to the actual condition of the SG was investigated through the numerical analysis of the experiment on water vapor discharging in liquid sodium. As shown in Fig. 8, the computational domain consists of the cylindrical vessel 884 mm in diameter and 1085 mm in height, the two simulated horizontal heat transfer tubes 525 mm in length and 32 mm in outer diameter, and its support plates. The distance between the two tubes is 68 mm. The cylindrical vessel was initially filled with liquid sodium at 522 °C and 0.15 MPa as with the experiment. There is a discharging nozzle closed with a rupture disk at the center of the downside tube. In the experiment, the water vapor which is pressurized and heated to the rated condition of the SG was supplied to the downside tube and goes into the sodium pool vertically upward through the nozzle. In the numerical analysis, there is an inflow boundary of the pressurized water vapor at the center of the downside tube. The inflow boundary simulates 8.2 mm-diameter discharging nozzle existing in the experimental apparatus. The experimental result showed that the time-averaged value of the temperature and the pressure inside the discharging tube was 374.4 °C and 17.17 MP. These values were used as the boundary conditions at the inflow boundary. The gas, liquid, and liquid droplet phases can go out from the top surface. The pressure on the top surface was assumed to be constant at 0.15 MPa. The all conditions of water vapor and liquid sodium shown here are equivalent to the conditions of the SG. The computational domain was divided into the unequally-spaced mesh. In order to reproduce the behavior of the underexpanded jet, the smallest mesh was placed between the two tubes.

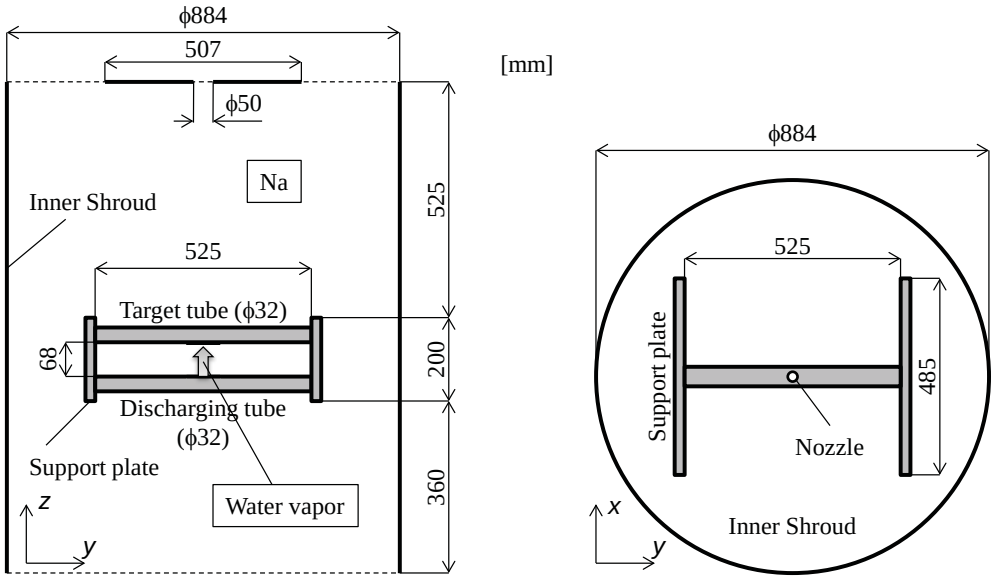

Vertical sectional view Horizontal sectional view

Figure 8. Computational domain for water vapor discharging in liquid sodium.

Figure 9 shows the time-averaged distributions of the gas-phase temperature, gas-phase velocity, liquid droplet velocity, void fraction, volume fraction of water vapor, volume fraction of hydrogen, and mass concentration of NaOH on a vertical plane intersecting with the center of the inflow boundary. As shown in Fig. 9(a), the high temperature region was formed around the reacting jet and the target tube by the chemical reaction. The calculated temperature distribution agreed with the measurement result well as described later. Occurrence of the chemical reaction can be confirmed from the distributions of the chemical species. As shown in Fig. 9(f), the water vapor disappears by the chemical reaction with increasing distance from the inflow boundary. Instead, the hydrogen and the NaOH become a main species of the gas phase (Figs. 9(g) and (h)). From Fig. 9(b), it can be seen that the air expands after exiting the nozzle. A Mach disk appears above the expansion zone. The gas-phase velocity reached up to the supersonic velocity and decreased behind the Mach disk. The high-velocity liquid droplet appeared around the underexpanded jet and impinged on the target tube. Figure 9(d) shows a photograph of the lower surface of the target tube. The wastage marks locate about 10 to 20 mm in an axial direction away from the center. Measurement of the surface shape showed that the wastage depth became maximum at the wastage mark. The impingement position of the high-velocity liquid droplet was close to the wastage mark. This implies that the SERAPHIM code has a capability to predict the environment of the LDIE.

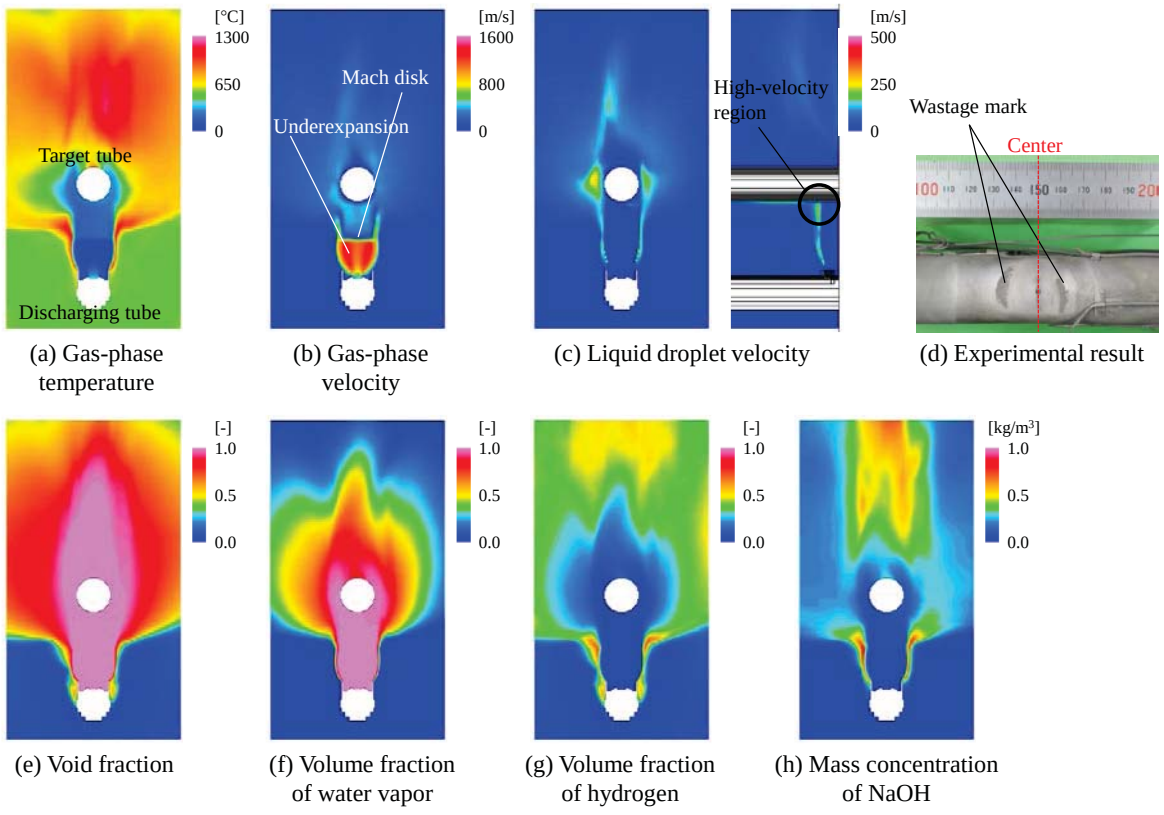

(a) Gas-phase temperature (b) Gas-phase velocity (c) Liquid droplet velocity (d) Experimental result

(e) Void fraction (f) Volume fraction of water vapor (g) Volume fraction of hydrogen (h) Mass concentration of NaOH

Figure 9. Numerical results of water vapor discharging in liquid sodium.

Figure 10 shows the positions of the thermocouples and the comparison of the temperature distribution. In the experiment, the thermocouples deformed by the effect of the reacting jet and the measuring point moved as shown in Fig. 10(a). The calculated weight-averaged temperature at the after-movement position is shown in Fig. 10(b). The weighted-averaged temperature is given by

$$T_w = \frac{\sum \alpha_i \rho_i T_i}{\sum \alpha_i \rho_i} \tag{18}$$

The experimental results in Fig. 10(b) shows an averaged value and a fluctuation range. At TC-1 and TC-5, both of the numerical and the experimental result is close to the initial temperature of liquid sodium since these positions locate out of reach of the reacting zone. TC-2, TC-4, TC-6, and TC-7 shows high temperature because of the chemical reaction. On the other hand, TC-3 indicates relatively low temperature since it is surrounded by the unreacted water vapor. The numerical analysis reproduced the tendency of the temperature distribution measured in the experiment. This implies that the SERAPHIM code can reproduce the temperature distribution formed by the multiphase flow including underexpanded jet and the chemical reaction.

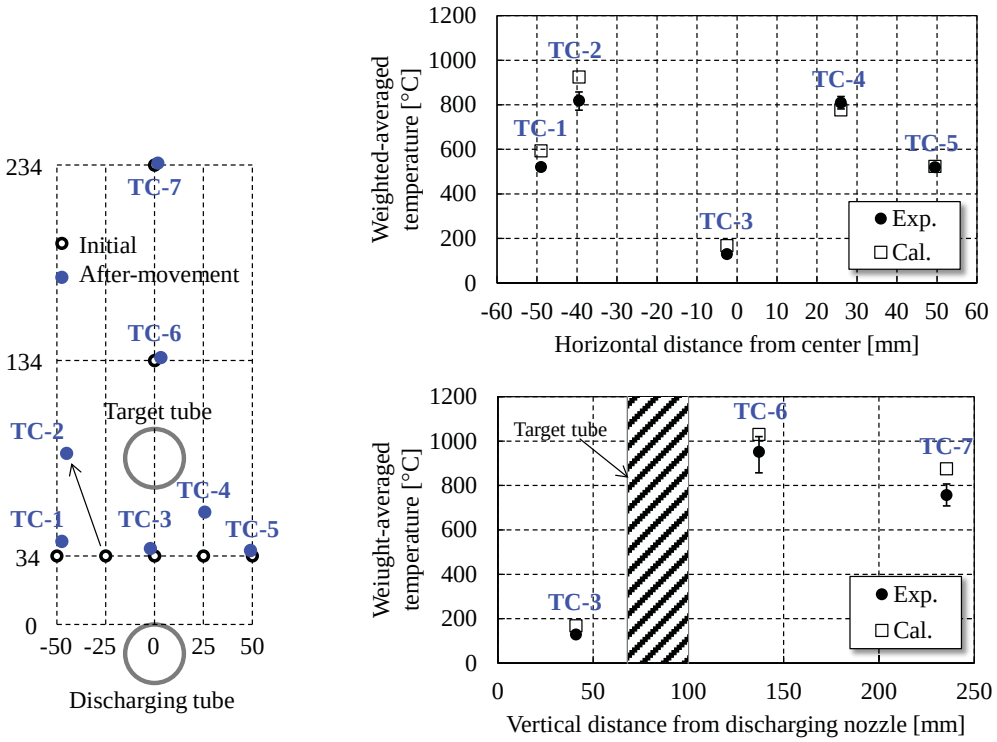

(a) T/C position (b) Temperature distribution

Figure 10. Comparison of temperature distribution.

4. CONCLUSIONS

For assessment of the wastage environment, a mechanistic computer code calculating compressible multicomponent multiphase flow with sodium-water chemical reaction has been developed. In this study, the numerical models for liquid droplet entrainment and its transport were newly developed and integrated into the SERAPHIM code. Applicability of the SERAPHIM code was investigated through the analysis of the experiment on liquid droplet entrainment at the surface of the water pool and the experiment on water vapor discharging in liquid sodium. It was demonstrated that the SERAPHIM code

could predict the temperature distribution and the environment of the LDIE under the actual condition of the SG.

ACKNOWLEDGMENTS

This work was supported by a study of “Development of Multi-Physics Evaluation System on Failure Propagation of Heat Transfer Tubes in the Steam Generator of Fast Breeder Reactor” entrusted to “Japan Atomic Energy Agency (JAEA)” by the Ministry of Education, Culture, Sports, Science and Technology of Japan (MEXT).

REFERENCES

1. T. Takata and A. Yamaguchi, “Numerical Approach to the Safety Evaluation of Sodium-water Reaction,” *J. Nucl. Sci. Technol.*, **40**(10), pp. 708-718 (2003).
2. T. Takata, et al., “Numerical Methodology of Sodium-water Reaction with Multiphase Flow Analysis,” *Nucl. Sci. Eng.*, **150**, pp. 221-236 (2005).
3. T. Takata, et al., “Computational Methodology of Sodium-water Reaction Phenomenon in Steam Generator of Sodium-cooled Fast Reactor,” *J. Nucl. Sci. Technol.*, **46**(6), pp. 613-623 (2009).
4. A. Uchibori, et al., “Numerical Analysis of Supersonic Gas Jets into Liquid Pools with or without Chemical Reaction Using the SERAPHIM Program,” *Nucl. Eng. Des.*, **249**, pp. 35-40 (2012).
5. H. Kudo, et al., “Visualization on the Behavior of Inert Gas Jets Impinging on a Single Glass Tube Submerged in Liquid Sodium,” *J. Nucl. Sci. Technol.*, **50**(1), pp. 72-79 (2013).
6. K. Arae, et al., “Evaluation of Wastage by Liquid Impingement Droplet Erosion in Steam Generation of Sodium-cooled Fast Reactor,” *Proceedings of 17th national symposium on power and energy systems (SPES 2012)*, Fukuoka, Japan, June 21-22 (2012).
7. M. Epstein, et al., “Liquid Entrainment by an Expanding Core Disruptive Accident Bubble - a Kelvin/Helmholtz Phenomenon,” *Nucl. Eng. Des.*, **210**, pp. 53-77 (2001).
8. C. W. Hirt and J. L. Cook, “Calculating Three-Dimensional Flows around Structures and over Rough Terrain,” *J. Comp. Phys.*, **10**, pp. 324-340 (1972).
9. F. P. Ricou and D. B. Spalding, “Measurements of Entrainment by Axisymmetrical Turbulent Jets,” *J. Fluid Mech.*, **11**, pp. 21-32 (1961).
10. R. B. Bell, et al., “The Structure of a Submerged Impinging Gas Jet,” *J. British Nuclear Energy Society*, **11**, pp. 183-193 (1972).
11. J. L. Carreau, et al., “Hydrodynamics of an Axisymmetric, Submerged Non-reactive Gas Jet-measurement of Entrainment Contribution to the Wastage Modeling,” *Proceedings of 20th Intersociety Energy Conversion Engineering Conference*, Miami Beach, FL, USA, **1**, pp. 688-695 (1985).
12. E. Loth and G. M. Faeth, “Structure of Underexpanded Round Air Jets Submerged in Water,” *Int. J. Multiphase Flow*, **15**, pp. 589-603 (1989).
13. E. Loth and G. M. Faeth, “Structure of Plane Underexpanded Air Jets into Water,” *AIChE J.*, **36**, pp. 818-826 (1990).
14. M. Epstein, et al., “Analytical Model for Peak Temperature within a Sodium-Water Reaction Jet,” *J. Nucl. Sci. Technol.*, **43**(1), pp. 43-54 (2006).
15. M. J. Walsh, “Influence of Particle Drag Coefficient on Particle Motion in High-speed Flow with Typical Laser Velocimeter Applications,” NASA TN D-8120 (1976).
16. M. Epstein, et al., “Establishment of Analytical Model for Peak Temperature within a Sodium-Water Reaction Jet, (II) Mean Droplet Size in a Submerged Gas Jet,” *J. Nucl. Sci. Technol.*, **42**(11), pp. 961-969 (2005).
17. T. Takata, et al., “Modification of Multi-dimensional Sodium-Water Reaction Analysis Code: SERAPHIM and Sensitivity Analyses on the Early Stage of Leakage”, JNC TN9400 2003-024 (2003). [in Japanese]

18. H. Tanabe, et al., “The Development and Application of Overheating Failure Model of FBR Steam Generator Tubes”, PNC TN9410 98-029 (1976). [in Japanese]
19. W. C. Rivard and M. D. Torrey, “Numerical Calculation of Flashing from Long Pipes Using a Two-fluid Model”, LA-NUREG-6330-MS (1976).